Electronic Supplementary Material (ESI) for Journal of Materials Chemistry C.

Supplementary Information for Resonance-Induced Anomalies in Temperature-Dependent Raman Scattering of $PdSe_2$

Omar Abdul-Aziz,[†] Daniel Wolverson,[‡] Charles Sayers,[¶] Ettore Carpene,[§] Fulvio Parmigiani,[‖] Hamoon Hedayat,[*,†] and Paul H. M. van Loosdrecht[*,†]

[†]*Universität zu Köln, II. Physikalisches Institut, Zülpicher Straße 77, Köln D-50937, Germany*

[‡]*Department of Physics and Centre for Photonics and Photonic Materials, University of Bath, BA2 7AY Bath, UK*

[¶]*Dipartimento di Fisica, Politecnico di Milano, 20133 Milan, Italy*

[§]*CNR-IFN, Dipartimento di Fisica, Politecnico di Milano, 20133 Milan, Italy*

[‖]*Dipartimento di Fisica, Università di Trieste, via A. Valerio 2, 34127, Trieste, Italy*

E-mail: hedayat@ph2.uni-koeln.de; pvl@ph2.uni-koeln.de

1. The FWHM of the A_g modes as a function of temperature

In the main maniuscript, we focused on the temperature-dependent amplitude and frequency of phonon modes. Figure S1 shows the line widths of all phonon modes as a function of temperature. It is evident that the line width of the A_g^2 phonon modes is significantly impacted by temperature. As expected, the line-widths remain nearly unchanged at lower

temperatures and then start to rise around 100 K, similar to the observed behavior of the phonon frequency shift. Therefore, the same explanation as discussed in the main text can be used to account for the temperature-dependent line widths of phonons.

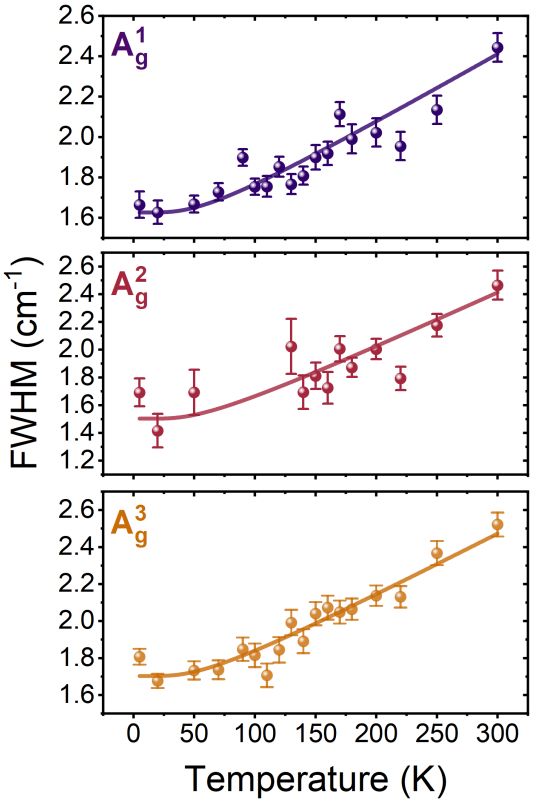

Figure S1: The full width at half maximum of the Raman peaks, as a function of temperature, of A_g^1, A_g^2, and A_g^3 modes. From 125 K down to 70 K, the A_g^2 mode exhibits zero intensity due to complete suppression. In each panel, we fit the data to the harmonic model characterized by the processes of optical phonon decay using Eq.S1 (solid lines).

The broadening of the Raman mode width, analogous to the softening of the Raman mode frequencies, is related to the anharmonic phonon interactions and can be described by the following relation:

$$\Gamma(T) = C + \Gamma_0 \left(1 + \frac{2}{e^x - 1}\right) \tag{S1}$$

Where $x = \frac{\hbar\omega_0}{2k_bT}$, Γ_0 is the anharmonic constant and C is peak broadening related to phonon confinement.[1] The parameters obtained from the fit of Eq.S1 to experimental data are pre-

sented in Table S1.

Table S1: The values of anharmonic constants obtained from the temperature-dependent analysis of the Raman mode FWHM of bulk $PdSe_2$ sample.

mode	C (cm^{-1})	Γ_0 (cm^{-1})
bulk		
A_g^1	1.3492 ± 0.19	0.2772 ± 0.022
A_g^2	1.1813 ± 0.25	0.3214 ± 0.042
A_g^3	1.4309 ± 0.15	0.2897 ± 0.033

2. Raman scattering in cross polarization configuration

Figure S2(a) illustrates the temperature-dependent Raman spectra of bulk $PdSe_2$ with excitation energy of 2.33 eV (532 nm) under close-to-cross-configuration (an incomplete cross configuration, where the angle between e_i and e_s is 75°). This configuration proves useful in understanding the interplay of phonons, since all phonon modes are observed simultaneously. The B_{1g} phonon modes are extracted by fitting the spectra with Lorentzian line shapes, revealing their temperature dependence.

In the temperature range of 300 to 5 K, the broad peak at 150 cm^{-1} undergoes a significant evolution, demonstrating a strong splitting of the A_g^1 and B_{1g}^1 modes. The in-plane phonon mode B_{1g}^2 exhibits pronounced softening, similar to the parallel configuration measurements for the A_g^2 mode. Conversely, the higher frequency B_{1g}^3 at 275 cm^{-1} experiences a notable enhancement as the temperature decreases.

The intensities of B_{1g}^1 and B_{1g}^3 increase continuously from 300 K, reaching maximum intensities at 120 K, while B_{1g}^2 decreases slowly, displaying a minimum intensity at 100 K, similar to the behavior of the A_g^2 mode. Figures S2(b), presents the B_{1g} phonon frequencies. Notably, the frequency of all examined B_{1g} modes blue-shifts with decreasing temperature, which then saturate at very low temperatures. Employing the same fitting procedure used for the frequencies of the A_g modes, the B_{1g} modes were fitted using the anharmonic approxima-

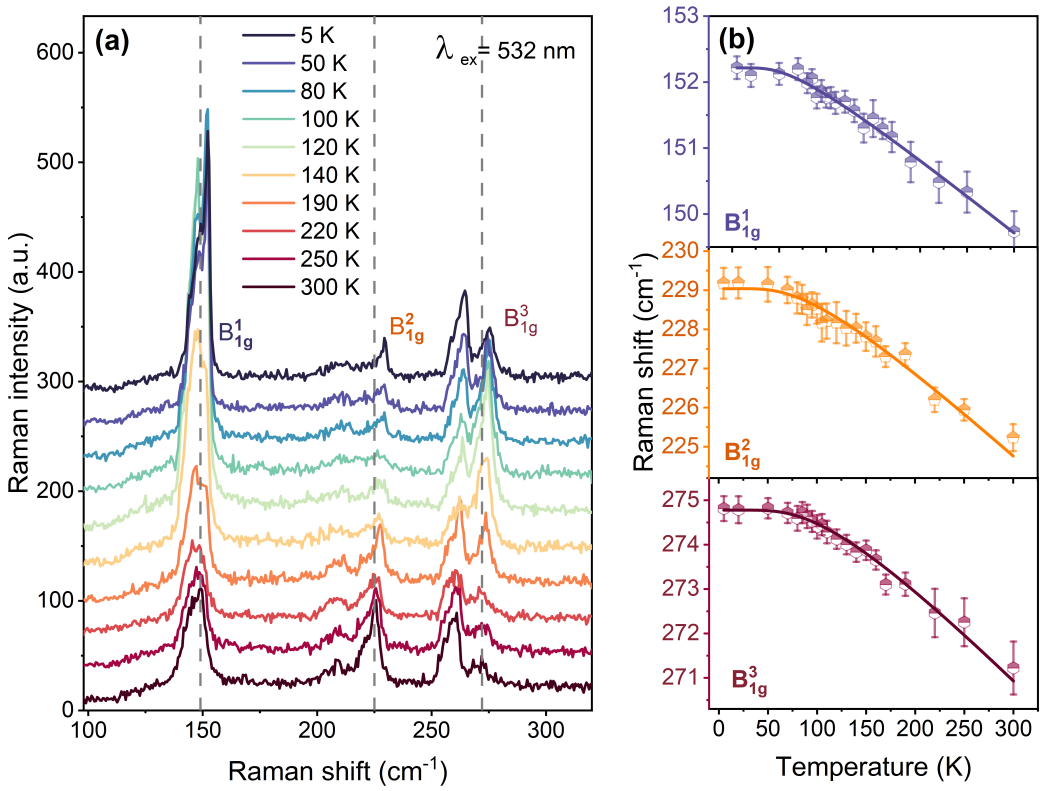

Figure S2: (a) Temperature-dependent Raman spectra of bulk $PdSe_2$ under close-cross-configuration with an excitation energy of 2.33 eV (532 nm). (d) Raman peak position as a function of temperature for the three B_{1g} phonon modes. In each panel, we fit the data to the anharmonic model characterization by the processes of optical phonon process decay (solid lines) using Eq.(1) in the main text over the entire temperature range 5 to 300 K.

tion for phonons, as explained using Eq.1 in the main text. The corresponding anharmonic constants are presented in Table 2 in the main text.

3. Trilayer sample

Figure S3(a) shows the Raman spectra at room temperature, of micro-mechanically exfoliated $PdSe_2$ trilayer sample on a SiO_2/Si substrate in both Parallel (xx) and cross (xy) polarized configurations for 2.33 eV excitation. Figures S3(b) and S3(c) show the optical image and the atomic force microscopy (AFM) of a trilayer $PdSe_2$ sample deposited on a SiO_2/Si substrate. The corresponding AFM of the thin flake shows a height profile of ∼2 nm,

consistent with the three-layer nature of the $PdSe_2$ exfoliated sample. The Raman data of the trilayer $PdSe_2$ reveal a phonon blueshift in both the A_g and B_{1g} modes of approximately 5-9 cm^{-1} as compared to the bulk sample, which is in excellent agreement with the other reports.[2,3] This large blueshift from bulk to trilayer is attributed to the strong interlayer coupling and the change of the in-plane lattice constants.

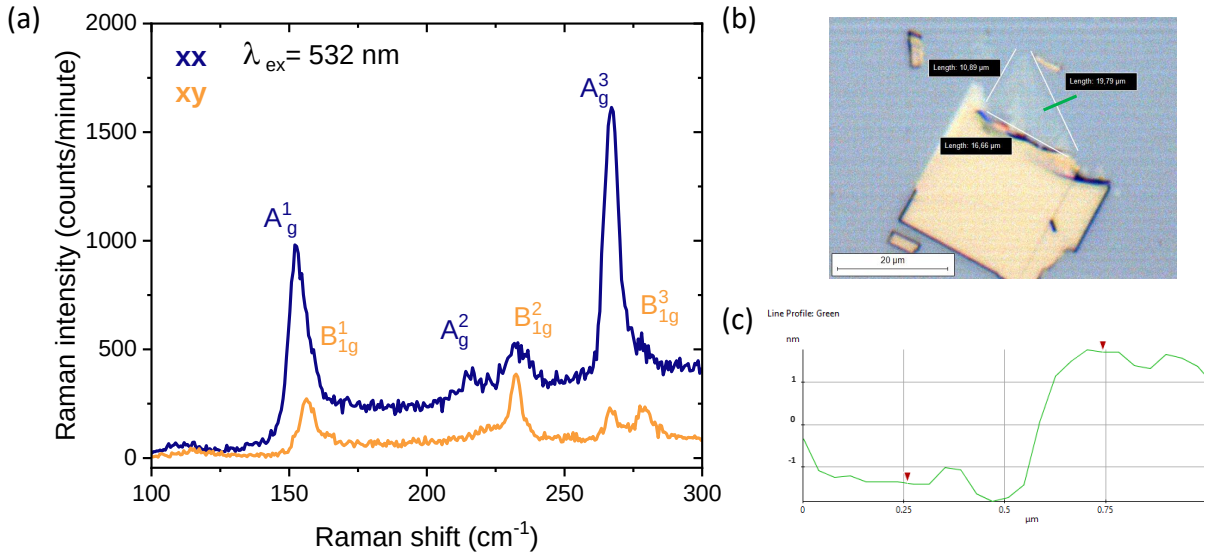

Figure S3: (a) Raman spectra of trilayer $PdSe_2$ in both parallel (blue line) and cross configurations (yellow line) measured at room temperature. Phonon modes are labeled with their irreducible representations. (b) An optical image of the exfoliated $PdSe_2$ sample, obtained through micromechanical exfoliation onto a SiO_2 /Si substrate with a 280 nm oxide layer, is shown. (c) The AFM image of the $PdSe_2$ flake is presented, and the line profile (green) confirms a thickness of 2 nm, establishing the three-layer nature of the exfoliated sample.

Figure S4(a) illustrates the Raman spectrum of the trilayer $PdSe_2$ sample for various temperatures. The Raman modes consistently exhibit a nonlinear blue shift as the temperature decreases, reaching a saturation point between 50 and 5 K. The associated anharmonic constants are detailed in Table 2 of the main text. The FWHM for all modes exhibits a consistent decrease with reducing temperature. This behavior is less pronounced in trilayer $PdSe_2$, where the strong softening observed in bulk in-plane phonon modes is absent.

In the bulk $PdSe_2$ sample, the room-temperature FWHM for the A_g and B_{1g} phonon modes

is less than 6 cm^{-1} for each mode, respectively. Yet, in the trilayer sample, larger FWHM values are observed, indicating broader peaks likely due to the presence of the film substrate and associated defects. Notably, the temperature-dependent anomalies observed in bulk $PdSe_2$, starting at 180 K, peaking at 120 K, and subsequently decreasing, are not as pronounced in the trilayer.

Despite these distinctions, the presence of B^3_{1g} is still discernible at higher frequency and lower temperatures (T lower than 130 K). This observation suggests a different origin for the substantial intensity change in A^1_g, along with the symmetry change indicated by the appearance of B^3_{1g} in the parallel configuration.

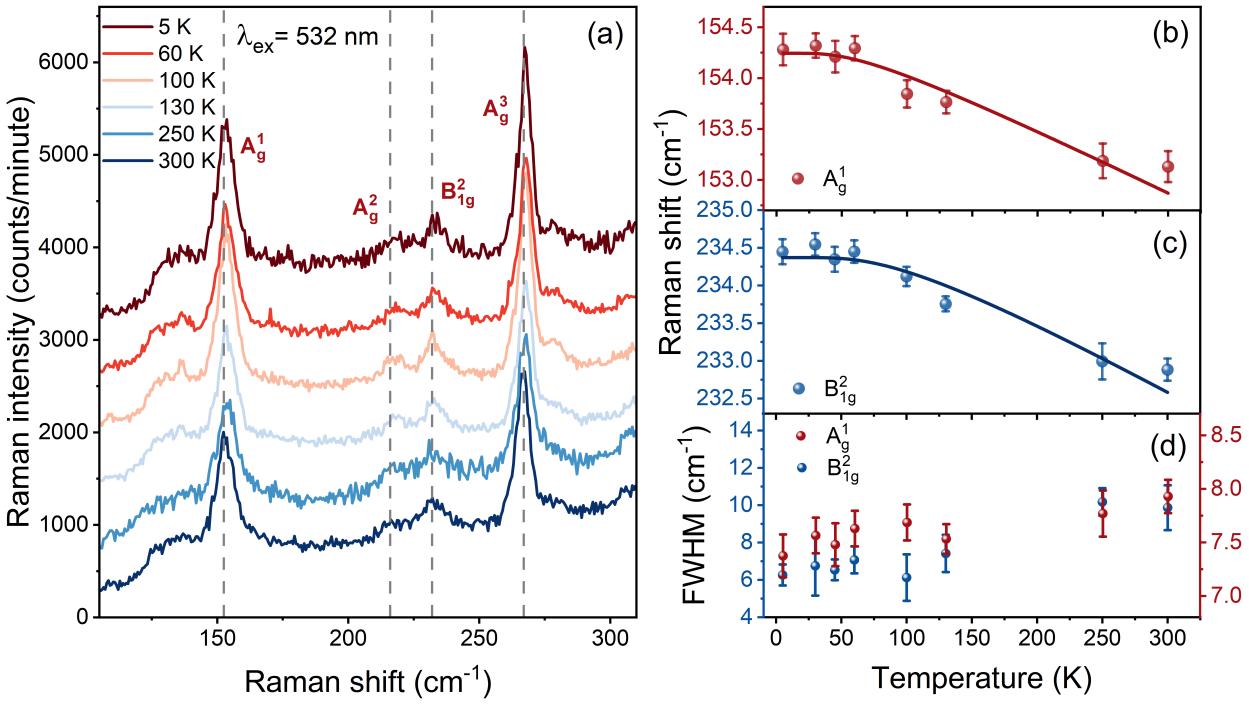

Figure S4: (a) Temperature-dependent Raman spectra of trilayer $PdSe_2$ under parallel configuration (xx). (b) and (c) Raman frequency as a function of temperature for the A^1_g and B^2_{1g} modes. In each panel, we fit the data to Eq.(1) (solid lines) from 5 to 300K. The fit is extrapolated over the entire temperature range. (d) The FWHM as a function of temperature for the A^1_g, and B^2_{1g} modes, respectively.

4. Angular dependence Raman scattering

The unit cell of the $PdSe_2$ crystal consists of two layers and 12 atoms; therefore, it has 36 normal phonon modes at the Γ point. The irreducible representation of the phonon modes can be expressed as

$$\Gamma_{\text{bulk}} = 3A_g + 3B_{1g} + 3B_{2g} + 3B_{3g} + 6A_u + 6B_{1u} + 6B_{2u} + 6B_{3u} \tag{2}$$

where only $3A_g$, $3B_{1g}$, $3B_{2g}$, and $3B_{3g}$ modes are Raman active.

The Raman tensors for the Raman active modes take the form below:

$$\begin{aligned} \tilde{R}(A_g) &= \begin{bmatrix} a & 0 & 0 \\ 0 & b & 0 \\ 0 & 0 & c \end{bmatrix}, \quad \tilde{R}(B_{1g}) = \begin{bmatrix} 0 & d & 0 \\ d & 0 & 0 \\ 0 & 0 & c \end{bmatrix}, \\ \tilde{R}(B_{2g}) &= \begin{bmatrix} 0 & 0 & e \\ 0 & 0 & 0 \\ e & 0 & 0 \end{bmatrix}, \quad \tilde{R}(B_{3g}) = \begin{bmatrix} 0 & 0 & 0 \\ 0 & 0 & f \\ 0 & f & 0 \end{bmatrix} \end{aligned} \tag{3}$$

where a to f are constant terms. In the experimental backscattering configuration, where the electric polarization of incident (e_i) and scattered (e_s) lights is in the plane (the x-y plane), the Raman intensity of a phonon mode is proportional to $I = |\vec{e}_s \cdot \tilde{R} \cdot \vec{e}_i|^2$. For the experimental backscattering configuration, e_i and e_s can be expressed as $e_i = (\cos\theta \ \sin\theta \ 0)$ and $e_s = (\cos\phi \ \sin\phi \ 0)$. The variables θ and ϕ represent the angles between the crystal orientation and the polarization direction of incident light or scattered light. Thus, the observed Raman intensities of the B_{2g} and B_{3g} modes are always zero. Only the A_g and B_{1g} modes exhibit distinct Raman intensities as a function of the polarization angles θ and ϕ. Therefore, Raman intensities of A_g modes versus the polarization angle under the parallel

configuration can be obtained as:

$$I(\mathrm{A_g})^p = (a\cos^2\theta + b\sin^2\theta)^2 \tag{4}$$

This is in good agreement with our results and previous reports.[4]

5. DFT and electron-phonon coupling calculations

The theoretically calculated values for each phonon mode are as follows: 142 cm^{-1} for A_g^1, 144 cm^{-1} for B_{1g}^1, 201 cm^{-1} for A_g^2, 222 cm^{-1} for B_{1g}^2, 253 ccm^{-1} for A_g^3, and 265 cm^{-1} for B_{1g}^3. It is important to note that the deviation from the experimental values is expected since the frequencies are systematically slightly underestimated at this level of DFT. To estimate Raman cross-sections and electron-phonon coupling for $PdSe_2$, we performed several calculations using Quantum Espresso[5,6] and VASP.[7] Here is a summary of the key points.

Raman tensors were calculated, including those for modes that are normally forbidden for backscattering from the layer surface. The results showed that, when listed in order of frequency, close-lying modes could exchange places depending on the exact calculation details. However, atomic displacements in the three types of calculation were found to be the same, ensuring that the modes were identifiable. The Raman tensor calculation was performed with Quantum Espresso.[8]

EPW (Electron-Phonon Wannier)[9,10] calculations were conducted using Quantum Espresso. The EPW calculation checked the interpolation scheme to ensure that the electronic and phonon bands were correctly reproduced, as shown in Figure 1(b) of the main text. The electron-phonon coupling at the Gamma point provided an indication of the Raman cross-section, shown in the next section.

VASP and phonopy[11,12] were used to investigate how frozen phonons modulate the band structure for each of the Raman modes. This analysis allowed for a simpler estimation of electron-phonon coupling, particularly the deformation potential, and provides additional

insight beyond the EPW results because the influence of specific phonons on the electronic transitions involved in the resonant Raman process is revealed (Figure 7 of the main text). It is important to note that the results from Quantum Espresso and VASP are not expected to be identical, mainly due to the use of different pseudopotentials in each case. For Quantum Espresso, ultrasoft pseudopotentials of PBE type[13] were used. Differences in mode frequencies should be expected, and consistency in atomic displacements ensures that modes can still be identified.

6. EPW calculations of the Raman modes

The results of the EPW calculations are depicted in Figure S5. These electron-phonon coupling strengths $\lambda_{q\nu}$ are summed over electronic states k and so do not highlight the role of any resonant transitions. However, the strengths shown correlate rather well with (i) the observed Raman intensities, (ii) the non-resonant Raman tensors calculated via DFPT, and (iii) the frozen-phonon results of Figure 7 in the main text. For example, in all cases, A_g^3 is predicted to dominate before resonant effects are taken into account.

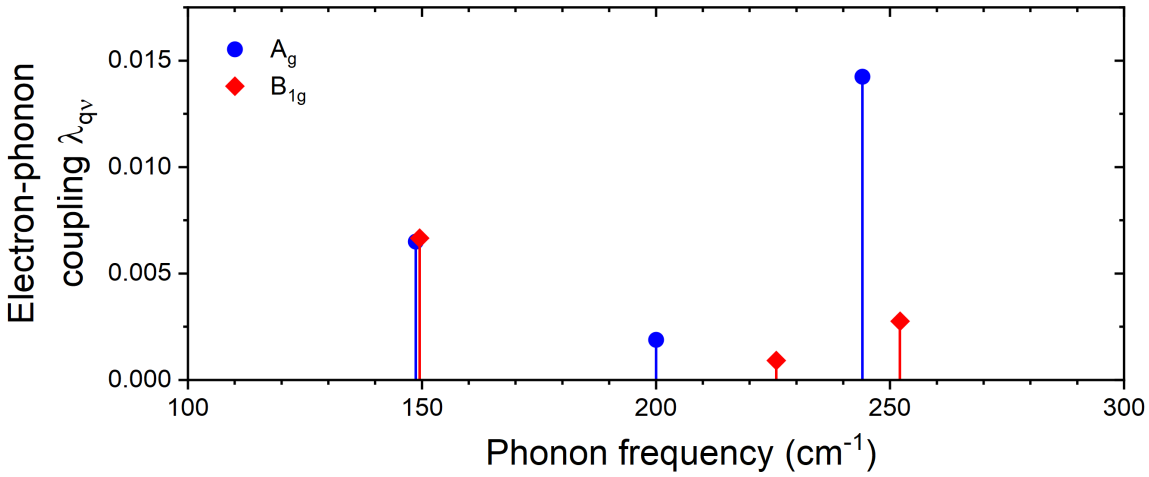

Figure S5: The results of EPW calculation of A_g and B_{1g} modes.

References

(1) Balkanski, M.; Wallis, R.; Haro, E. Anharmonic effects in light scattering due to optical phonons in silicon. *Phys. Rev. B* **1983**, *28*, 1928.

(2) Oyedele, A. D.; Yang, S.; Liang, L.; Puretzky, A. A.; Wang, K.; Zhang, J.; Yu, P.; Pudasaini, P. R.; Ghosh, A. W.; Liu, Z., et al. $PdSe_2$: pentagonal two-dimensional layers with high air stability for electronics. *J. Am. Chem. Soc.* **2017**, *139*, 14090–14097.

(3) Yu, J.; Kuang, X.; Li, J.; Zhong, J.; Zeng, C.; Cao, L.; Liu, Z.; Zeng, Z.; Luo, Z.; He, T., et al. Giant nonlinear optical activity in two-dimensional palladium diselenide. *Nat. Commun* **2021**, *12*, 1083.

(4) Yu, J.; Kuang, X.; Gao, Y.; Wang, Y.; Chen, K.; Ding, Z.; Liu, J.; Cong, C.; He, J.; Liu, Z., et al. Direct observation of the linear dichroism transition in two-dimensional palladium diselenide. *Nano Lett.* **2020**, *20*, 1172–1182.

(5) Giannozzi, P. et al. QUANTUM ESPRESSO: a modular and open-source software project for quantum simulations of materials. *J Phys. Condens. Matter* **2009**, *21*.

(6) Baroni, S. Phonons from density-functional perturbation theory. *Abstr. Pap. Am. Chem. Soc.* **1997**, *213*, 277–Comp.

(7) Hafner, J. Ab initio simulations of materials using VASP:: Density-functional theory and beyond. *J. Comput. Chem.* **2008**, *29*, 2044–2078.

(8) Baroni, S.; de Gironcoli, S.; Dal Corso, A.; Giannozzi, P. Phonons and related crystal properties from density-functional perturbation theory. *Rev. Mod. Phys.* **2001**, *73*, 515–562.

(9) Giustino, F.; Cohen, M. L.; Louie, S. G. Electron-phonon interaction using Wannier functions. *Phys. Rev. B* **2007**, *76*.

(10) Poncé, S.; Margine, E. R.; Verdi, C.; Giustino, F. EPW: Electron-phonon coupling, transport and superconducting properties using maximally localized Wannier functions. *Comput. Phys. Commun.* **2016**, *209*, 116–133.

(11) Togo, A.; Tanaka, I. First principles phonon calculations in materials science. *Scr. Mater.* **2015**, *108*, 1–5.

(12) Togo, A. First-principles Phonon Calculations with Phonopy and Phono3py. *JPSJ* **2023**, *92*.

(13) Perdew, J. P.; Burke, K.; Wang, Y. Generalized gradient approximation for the exchange-correlation hole of a many-electron system. *Phys. Rev. B* **1996**, *54*, 16533–16539.